

QUANTITATIVE, THREE-DIMENSIONAL ANALYSIS OF THE GLOBAL CORONA WITH MULTI-SPACECRAFT DIFFERENTIAL EMISSION MEASURE TOMOGRAPHY

RICHARD A. FRAZIN¹, ALBERTO M. VÁSQUEZ², AND FARZAD KAMALABADI³

¹ Department of Ocean, Atmospheric and Space Science, University of Michigan, Ann Arbor, MI 48109, USA; rfrazin@umich.edu

² Instituto de Astronomía y Física del Espacio, CONICET-University of Buenos Aires, Ciudad de Buenos Aires, CC 67 - Suc 28, Argentina; albert@iafe.uba.ar

³ Department of Electrical and Computer Engineering, University of Illinois, Urbana, IL 61801, USA; farzadk@uillinois.edu

Received 2009 March 24; accepted 2009 June 12; published 2009 July 24

ABSTRACT

A previous paper (Frazin et al. 2005b) introduced the concept of differential emission measure tomography (DEMT), which is a three-dimensional (3D) extension of the classical differential emission measure technique for determining the distribution of temperatures in a volume of plasma. The information for the reconstruction in the three spatial dimensions is provided by solar rotation and/or multi-spacecraft views. This paper describes, quantitatively, the procedure for implementing DEMT with data from NASA’s *STEREO*/EUVI instrument, including the radiometry, line-of-sight geometry, and image preparation steps. An example of a quantitative, multiband, 3D reconstruction and local differential emission measure curves are given, and it is demonstrated that, when applicable, DEMT is a simple 3D analysis tool that obviates the need for structure-specific modeling.

Key words: Sun: corona – Sun: prominences – Sun: UV radiation

Online-only material: color figures

1. INTRODUCTION

Differential emission measure tomography (DEMT) is the only three-dimensional (3D) technique for reconstructing the differential emission measure (DEM) in the Sun’s corona, and has the useful property of being global, i.e., reconstructing the entire corona at once. The DEMT concept was introduced by Frazin et al. (2005b; henceforth FKW05) and the first results from applying DEMT to data were reported in Vásquez et al. (2009), which discusses the coronal cavities overlying polar crown filaments. These papers, as well as Frazin & Kamalabadi (2005), review previous work on DEM as well as 3D reconstruction of the extreme-ultraviolet (EUV) corona. The basic theory of DEMT is explained and previous work is reviewed in FKW05, however that work was theoretical and did not consider the problem of combining measurements from different spacecraft or physically meaningful units. The purpose of this paper is to explain the theoretical basis and full methodology of DEMT with examples. We describe, quantitatively, the procedure for implementing DEMT with data from NASA’s *STEREO*/EUVI instrument.

The most important limitations of DEMT are as follows.

1. Temporal variations of the corona that occur on timescales shorter than can be resolved by the tomography method, which is roughly two weeks (although see Frazin et al. (2005a) for a discussion of dynamic tomography with Kalman filters). Using multiple spacecraft data sets can greatly reduce this time period and lessen the problem. Also, movies made from EUV or X-ray images can be used to identify regions that have no observable dynamics on spatial scales resolved by the tomographic grid.
2. The wings of the instrument point-spread function may prevent the analysis of fainter regions such as coronal holes or some objects above the limb, because an unknown amount of the signal is from other structures located elsewhere in the image. This issue has been addressed for the *TRACE* instrument by DeForest et al. (2009).

3. A small number of EUV and/or X-ray bands can preclude a unique DEM inversion (e.g., Schmelz et al. 2007), although the fully 3D analysis may help because the DEM in a small region, confined in height, may be narrower than the DEM over a full LOS.

Of course, these last two items are equally problematic for both standard DEM analysis and DEMT. Unlike other 3D reconstruction methods (e.g., Aschwanden et al. 2009), this technique divides the corona into “small” volumes and determines the average properties of the plasma inside those volumes, so there is no need for background subtraction and other modeling (which can be time consuming and complicated) to interpret line-of-sight (LOS) effects.

2. RADIOMETRY

This section relates the signal measured by the Extreme UltraViolet Imager (EUVI; Howard et al. 2008) to the desired physical units of the solar radiation. Noise is also discussed. Following the radiometry discussion in Born & Wolf (1999), consider a region of solar plasma emitting light, some of which is collected by an imaging telescope. A pixel on the telescope’s detector has an area A_p which subtends a solid angle $\Omega_p = A_p/f^2$, where f is the (effective) telescope focal length (in the case of EUVI, $A_p \approx (0.0135 \text{ mm})^2$ and $f \approx 1750 \text{ mm}$). The optical system places an image of a patch of solar plasma onto the pixel. This patch subtends the same solid angle $\Omega_p = A_s/d_s^2$, where A_s is the *projected* area of the plasma patch (i.e., A_s includes the cosine of the angle between the normal to the patch and the direction toward the telescope), and d_s is the distance of the patch to the telescope. The telescope entrance aperture has an area A_T ($A_T = 6.7 \text{ cm}^2$ for each EUVI quadrant). Since the normal to the entrance aperture is assumed to be pointed at the Sun, the telescope subtends a solid angle $\Omega_T = A_T/d_s^2$, as seen from the patch. The specific intensity emerging from the patch is $J(\lambda)$ and has units ($\text{ph}/\text{cm}^2 \text{ sr s } \text{\AA}$). The flux of photons from the patch entering the telescope aperture is $F(\lambda) = J(\lambda)A_s\Omega_T$, which has units ($\text{ph}/\text{s } \text{\AA}$). Using the above expressions for Ω_p

and Ω_T , one can eliminate A_s and d_s^2 and obtain the photon flux as

$$F(\lambda) = J(\lambda)\Omega_p A_T. \quad (1)$$

Thus, the incident photon flux has been expressed as a function of only the specific intensity and telescope properties with no dependence on the Sun–telescope distance.

The telescope has a wavelength-dependent optical efficiency factor for the k th EUV or X-ray filter, which we will denote as $\epsilon_k(\lambda)$. Let the telescope have K filters, so $0 \leq k \leq K - 1$. The efficiency factor is unitless and $0 \leq \epsilon_k(\lambda) \leq 1$. It is $\epsilon_k(\lambda)$ that creates the sharply peaked wavelength response (see below for the definition of the closely related *bandpass functions*). The product of the optical efficiency and the telescope area, i.e., $A_T \epsilon_k(\lambda)$ is called the *effective area*. The signal seen in the j th detector pixel with the k th filter in the optical path, $I_{k,j}$, has units of (dn/s) (“dn” is an instrument-specific unit and stands for “digital number”). The detector has a wavelength-dependent dn-to-photon conversion factor $p(\lambda)$, which has units of (dn/ph). For EUVI, $p(\lambda) = (e[\text{eV}]/3.65)/15$, where $e[\text{eV}]$ is the photon energy in electron volts. The signal seen in the j th detector pixel with the k th filter is given by

$$I_{k,j} = \int_0^\infty d\lambda \epsilon_k(\lambda) p(\lambda) F_j(\lambda) + n_{j,k}, \quad (2)$$

where $n_{j,k}$ represents noise in the data and the pixel index j has been used to subscript $F(\lambda)$ because the flux seen by the detector varies from one pixel to the next, according the spatial distribution of the coronal emission. Using Equation (1), this becomes

$$I_{k,j} = \Omega_p \int_0^\infty d\lambda A_T \epsilon_k(\lambda) p(\lambda) J_j(\lambda) + n_{j,k}. \quad (3)$$

We now define the *total instrument response* as

$$\Phi_k(\lambda) \equiv \Omega_p A_T \epsilon_k(\lambda) p(\lambda), \quad (4)$$

so that Equation (2) becomes

$$I_{k,j} = \int_0^\infty d\lambda \Phi_k(\lambda) J_j(\lambda) + n_{j,k}. \quad (5)$$

It is convenient to rewrite the total instrument response in normalized form as

$$\Phi_k(\lambda) = \Phi_{k,0} \phi_k(\lambda), \quad (6)$$

where the *bandpass function* $\phi_k(\lambda)$ is unitless and $0 \leq \phi_k(\lambda) \leq 1$, and $\Phi_{k,0}$ is the maximum value of the function $\phi_k(\lambda)$. Figure 1 shows a plot of the EUVI bandpass functions for both spacecraft. As can be seen, the differences between bandpass functions for the two spacecraft are small. Explicitly, the normalization factor is

$$\Phi_{k,0} \equiv \Omega_p A_T \epsilon_k(\lambda_0) p(\lambda_0), \quad (7)$$

where λ_0 is the wavelength at which the product $\epsilon_k(\lambda) p(\lambda)$ attains its maximum value. Note that $\Phi_{k,0}$ has units (dn sr cm²/ph). The constant $\Phi_{k,0}$ depends on the sensitivity of the specific instrument making the measurement. With the bandpass function and normalization factor so defined, Equation (5) becomes

$$I_{k,j} = \Phi_{k,0} \int_0^\infty d\lambda \phi_k(\lambda) J_j(\lambda) + n_{j,k}. \quad (8)$$

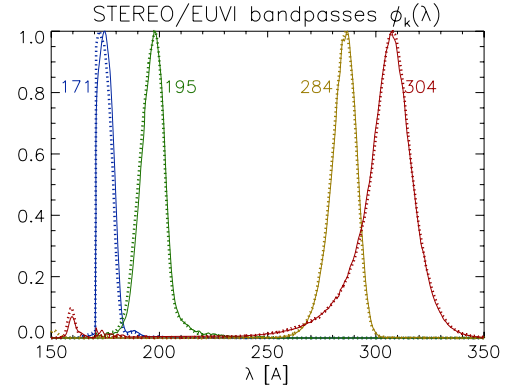


Figure 1. Laboratory measurements of the bandpass functions (see Equation (6)) for all four EUV bands of the EUVI instruments on *STEREO* A (solid) and B (dotted) spacecraft. For each band, the differences between both spacecraft are small, with the largest difference being near the peak of the 171 Å curves. The differences between the curves have a negligible effect on the temperature responses (see also Figure 2).

(A color version of this figure is available in the online journal.)

The noise in the EUVI instrument tends to be dominated by photon statistics (a Poisson process), however, the CCD produces a random number (~ 11 – 19) of electrons per detected photon (15 electrons/DN), and there is about 0.5 DN (1σ) read noise (on top of the constant bias, which is subtracted). Due to the low temperature (200 K) of the CCD, the thermal noise is thought to be negligible. The EUVI data are also altered by the lossy on-board ICER compression (Kiely & Klimesh 2003), which introduces “noise” due to word truncation and other artifacts (e.g., regions of constant intensity, especially off the disk where count rates are lower; J.-P. Wuelser 2008, private communication). Note that one of the properties of lossy compression is the creation of statistical correlations in the pixel-to-pixel noise properties. Deconvolution of the EUVI point-spread function taking the ICER compression into account currently is the subject of one of Frazin’s investigations. Deconvolution of the *TRACE* instrument point-spread function is treated in DeForest et al. (2009).

3. THE FILTER BAND EMISSIVITY

In an optically thin plasma, the specific intensity is given by an LOS integral of the emissivity $\eta(\mathbf{r}, \lambda)$, which has units (ph/cm³ sr s Å)

$$J_j(\lambda) = \int_{\text{LOS}} dl \eta(\mathbf{r}_j(l), \lambda), \quad (9)$$

where l is the distance along the LOS and $\mathbf{r}_j(l)$ is given by Equation (E1) (evaluated in the third coordinate system in Appendix E). Equations (8) and (9) can be combined into

$$I_{k,j} = \Phi_{k,0} \int_{\text{LOS}} dl \int_0^\infty d\lambda \phi_k(\lambda) \eta(\mathbf{r}_j(l), \lambda) + n_{j,k}. \quad (10)$$

The wavelength integral in Equation (10) can be used to define an emissivity-type quantity that has the bandpass function included. We will call this quantity the filter band emissivity (FBE), defined to be

$$\zeta_k(\mathbf{r}) \equiv \int_0^\infty d\lambda \phi_k(\lambda) \eta(\mathbf{r}, \lambda), \quad (11)$$

with units (ph/cm³ sr s). Using Equation (11) in Equation (10), we obtain the equation which forms the basis for tomographic reconstruction:

$$I_{k,j} = \Phi_{k,0} \int_{\text{LOS}} dl \zeta_k(\mathbf{r}_j(l)) + n_{k,j}. \quad (12)$$

The aim of the tomography is to invert Equation (12) in order to estimate $\zeta_k(\mathbf{r})$. One can learn about the physical properties of the plasma in three dimensions after $\zeta_k(\mathbf{r})$ has been estimated for a number of different filters, indexed by k .

When the electrons have a velocity distribution characterized by a temperature T , the emissivity can be expressed as (Young et al. 2003)

$$\eta(\mathbf{r}, \lambda) = N_e^2(\mathbf{r}) \psi(N_e(\mathbf{r}), \mathbf{a}(\mathbf{r}), T(\mathbf{r}); \lambda), \quad (13)$$

where \mathbf{a} is the vector of relevant elemental abundances and ψ , which has units (cm³ ph/sr s Å), is an emission function that depends on the atomic physics of the emission process. We assume only collisionally excited emission. Resonantly scattered components are discussed in Appendix D. Note that η is approximately proportional to N_e^2 and the remaining density sensitivity in ψ is quite weak in bands used by EUV and X-ray images, although high-resolution spectra can be used to identify spectral line pairs that make useful density diagnostics (e.g., Mariska 1992; Landi & Feldman 2008). Note that all of the spatial dependence is through N_e , \mathbf{a} , and T . Using Equation (11), we can rewrite the FBE in Equation (12) as

$$\zeta_k(\mathbf{r}) = N_e^2(\mathbf{r}) \int_0^\infty d\lambda \phi_k(\lambda) \psi(N_e(\mathbf{r}), \mathbf{a}(\mathbf{r}), T(\mathbf{r}); \lambda). \quad (14)$$

In Vázquez et al. (2009), we used the CHIANTI code (Young et al. 2003) to calculate the emissivity. CHIANTI computes the specific intensity in units of (ph/cm² sr s Å). One must specify the abundance mix, the electron density N_e , and the emission measure $\text{EM} = \log_{10} N_e^2 L$, where L is the column length. Choosing $L = 1$ cm allows one to fix the density, and also numerically equates the computed specific intensity to the desired emissivity.

4. THE TOMOGRAPHIC PROBLEM

The first step in the tomographic process is to discretize the volume of the corona (between, say, the coronal base at 1.0 and 1.25 R_s) on a computation grid. The computation grid contains M volume elements $\{V_i\}$ (called *voxels*), so $0 \leq i \leq M-1$. Under the assumption that the FBE is constant inside each volume element, Equation (12) can be expressed as a discrete sum over the FBEs in each voxel along the LOS:

$$I_{k,j} \approx \sum_i W_{k,j,i} \zeta_{k,i} + n_{k,j}, \quad (15)$$

where $I_{k,j}$ and $n_{k,j}$ have been redefined (with the corresponding change in units) as $I_{k,j} \rightarrow I_{k,j}/\Phi_{k,0}$ and $n_{k,j} \rightarrow n_{k,j}/\Phi_{k,0}$. Here, $\zeta_{k,i}$ is the average value of the FBE $\zeta_k(\mathbf{r})$ for all \mathbf{r} inside voxel i (see Equation (C1)), $\mathbf{W}_k \equiv \{W_{k,j,i}\}$ is a $J \times M$ matrix, with units (cm), corresponding to the length of the piece of the j th LOS that lies within the i th voxel, and J is the total number of pixels in all of the images (e.g., if each image has Q^2 pixels and there are P images then $J = PQ^2$, and $0 \leq j \leq J-1$). Specifically,

$$W_{k,j,i} = l_{k,j,i}, \quad (16)$$

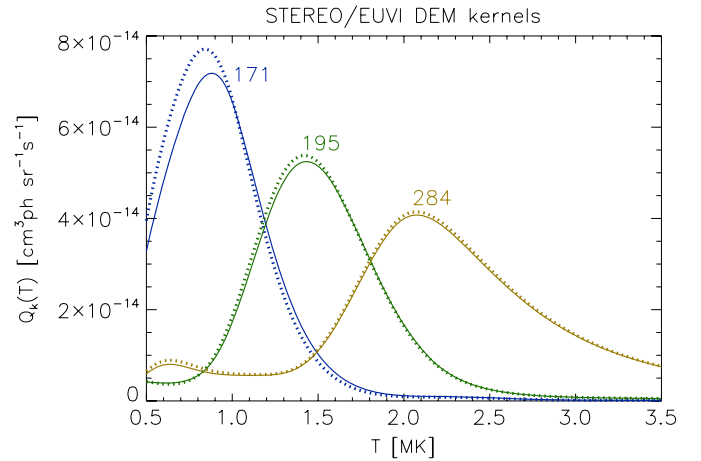


Figure 2. DEM kernels (see Equation (22)) for the 171, 195, and 284 Å bands of the EUVI instruments on *STEREO* A (solid) and B (dotted) spacecraft. The differences between the corresponding A and B curves are small, with the largest being observed around the peak of the 171 Å curves, for which discrepancies of order 7% or less are seen. These differences follow from those in the bandpass functions shown in Figure 1.

(A color version of this figure is available in the online journal.)

where $l_{k,j,i}$ is the path length of the j th LOS through the i th volume element of the computation grid. \mathbf{W}_k for this application differs from its counterpart in white-light tomography because it does not contain a Thomson scattering factor. Note that the vast majority of the $W_{k,j,i}$ will be zero since any particular LOS only intersects a small fraction of the voxels, which allows sparse matrix routines to be used (Frazin & Janzen 2002, henceforth FJ02). For each filter band k , Equation (15) can be expressed as

$$\mathbf{I}_k = \mathbf{W}_k \boldsymbol{\zeta}_k + \mathbf{n}_k, \quad (17)$$

where \mathbf{I}_k is the vector of all intensity measurements for the k th filter, $\boldsymbol{\zeta}_k \equiv \{\zeta_{k,j}\}$ and the vector $\mathbf{n}_k \equiv \{n_{k,j}\}$. Equation (17) and the statistics of \mathbf{n}_k define an independent tomographic inversion problem for each index value k . The multi-spacecraft formulation of Equation (17) is given in Appendix B.

4.1. Tomographic Reconstruction

Inverting Equation (17) to obtain $\boldsymbol{\zeta}_k$ can be done under the assumption that the corona is unchanging during data acquisition period, which is called the *static assumption*. This premise can be relaxed, allowing the reconstruction to be a function of time. In that case, all of the intensity measurements need to be indexed by their time bins t and the FBE vector also becomes a function of time. Adding the time-bin subscripts to Equation (17), it becomes

$$\mathbf{I}_{k,t} = \mathbf{W}_{k,t} \boldsymbol{\zeta}_{k,t} + \mathbf{n}_{k,t}. \quad (18)$$

This must now be supplemented by an evolution equation

$$\boldsymbol{\zeta}_{k,t+1} = \mathbf{F}_{k,t} \boldsymbol{\zeta}_{k,t} + \mathbf{v}_{k,t}, \quad (19)$$

where $\mathbf{F}_{k,t}$ is a (possibly nonlinear) time-stepping operator and $\mathbf{v}_{k,t}$ is a random process that accounts for unknown and/or poorly understood portion of the temporal evolution. Thus, the solution of Equations (18) and (19) becomes a function of time. Dynamic reconstruction in tomography of the corona is discussed in Frazin et al. (2005a), Butala et al. (2008), and Butala et al. (2009). The presently available solution methods are based on stochastic approximations to the Kalman

filter, so-called ensemble Kalman Filters (e.g., Evensen 2007; Butala et al. 2009), and an optimization scheme called 4DVAR (e.g., Daley 1991). This class of solution methods allows both causal and noncausal estimation. M. D. Butala et al. (2009, in preparation) have shown that dynamic solutions have greatly reduced reconstruction artifacts when compared to static solutions.

Under the static assumption, the inversion can be accomplished by minimizing the objective function

$$\hat{\zeta}_k = \underset{\zeta_k}{\operatorname{argmin}} \{ \|I_k - \mathbf{W}_k \zeta_k\|^2 + G(\mathbf{p}_k; \zeta_k) \}, \quad (20)$$

where $G(\mathbf{p}_k; \bullet)$ is a regularization functional that suppresses spurious high-frequency artifacts due to the poorly conditioned or singular nature of \mathbf{W}_k , and \mathbf{p}_k is a vector of parameters that control the amplitude and form of G . Regularization in the context of tomography is reviewed in Demoment (1989), Frazin (2000), FJ02, Frazin et al. (2007) and references therein. In Vázquez et al. (2009), we used the simple quadratic form $G(\mathbf{p}_k; \zeta_k) = p \|\mathbf{R} \zeta_k\|^2$, where \mathbf{R} is a finite difference matrix made to approximate second derivatives in the angular directions and p is the sole regularization parameter (controlling the amplitude in this case). The value of p , assumed the same for all k , was chosen via a statistical procedure called cross validation (Golub et al. 1979; FJ02). The redundancy in multi-spacecraft observations (i.e., viewing the Sun from the same angle at different times from different spacecraft), such as analyzed here, offers additional cross-validation opportunities not available in with data sets from a single spacecraft.

Since Equation (17) does not account for the Sun's temporal variations, coronal dynamics in one voxel can cause artifacts in neighboring voxels, including negative values of the statically reconstructed emissivity ζ_k (if the solution is not constrained to be positive). Examples of this effect in typical EUVI reconstructions can be seen in Figure 3. They are identical in nature to the zero-density artifacts (ZDAs) in white-light tomography (FJ02; Frazin et al. 2007). The requirement for accurate static reconstruction is that a given structure and its surroundings are stable in the time that they are seen by the telescopes (this is about two weeks in the single spacecraft case). Due to dynamics of the corona and the fact that solar rotation is utilized to provide the angular coverage, the issues of spatial resolution, temporal resolution, and artifacts are closely coupled. In the context tomographic reconstruction of N_e from LASCO-C2 pB data, Frazin et al. (2007) explored the effect of observation cadence on the spatial resolution of the reconstruction. They showed that as the cadence of pB images increases beyond 1 per day, the spatial resolution of the reconstruction increases, but there is a saturation point beyond which a higher cadence leads to no improvement, because the resolution is ultimately limited by smearing caused by the dynamics in the 14 day data acquisition period. It is postulated that with more spacecraft reducing the data acquisition time, the attainable spatial resolution improves, requiring a higher observation cadence to achieve that resolution (Frazin et al. 2007).

5. THE LOCAL DIFFERENTIAL EMISSION MEASURE

The FBE $\zeta_{k,i}$ in voxel i can be written in terms of the local differential emission measure (LDEM) $\xi_i(T)$, which has units

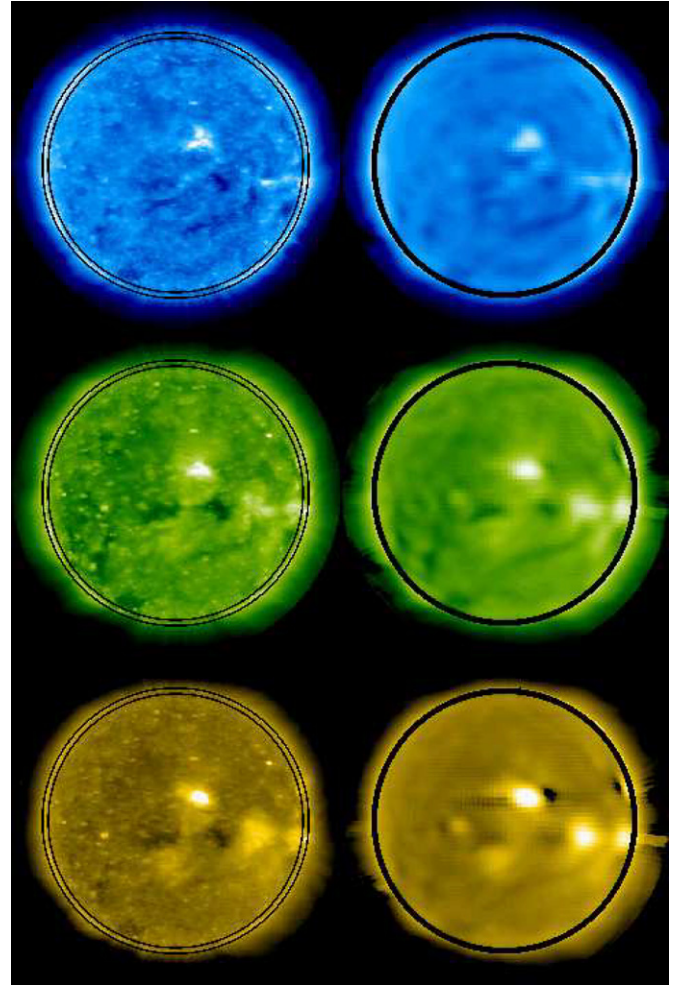


Figure 3. Left column shows examples of the time-binned (see Section A) EUVI-A images in the 171, 195, and 284 Å bands, taken near 20:00 UT on 2008 April 29. The right column displays the corresponding synthetic images calculated by integrating the tomographic models along the LOS of each pixel. In both cases, we show the logarithm of the intensity. The two columns use a common color scale for each band. The black streaks seen in the reconstructed images near some of the ARs (especially in the 284 Å band) are artifacts caused by the Sun's temporal variability. The thin black circles around the limb in the data images (left column) indicate the limits of the rejected data (see Appendix D), the black annuli (covering the region between 0.98 and $1.025 R_\odot$) in the synthetic images (right column) block the rejected regions, where we do not attempt to reproduce the observed intensities.

(A color version of this figure is available in the online journal.)

($\text{cm}^{-6} \text{ K}^{-1}$), as follows:

$$\zeta_{k,i} = \int dT Q_k(T) \xi_i(T), \quad (21)$$

where $Q_k(T)$ is the DEM kernel function defined as

$$Q_k(T) = \int d\lambda \phi_k(\lambda) \psi(N_{e0}, \mathbf{a}_0, T; \lambda), \quad (22)$$

in which N_{e0} is a reference density whose exact value is of little importance (see Section 3), and \mathbf{a}_0 is a reference set of abundances. $Q_k(T)$ has units ($\text{cm}^3 \text{ ph/sr s}$). As explained in Appendix C, where Equation (21) is derived, $\xi_i(T)$ is a function of (electron) temperature and is a measure of the amount of plasma within voxel i that is at temperature T . Thus, even though the spatial resolution of the tomographic reconstruction

is limited by the grid size, the LDEM gives information about the distribution of flux tube temperatures at subgrid spatial scales. The (spatial) mean square electron density in voxel i can be obtained by integrating the LDEM over temperature, i.e.,

$$\langle N_e^2 \rangle_i = \int dT \xi_i(T) \quad (23)$$

as shown in Equation (C19). Note that this density is inversely proportional to the assumed Fe abundance for bands dominated by Fe lines.

The emission function ψ most sensitively depends on the electron temperature T , largely due to the ionization equilibrium. While the dependence on N_e is quite weak, the emission of any particular spectral line is directly proportional to the abundance of the emitting species, making the dependence on the abundance vector \mathbf{a}_0 nontrivial. Coronal abundances tend to vary by a factor of several (e.g., Raymond et al. 1997), while the temperature sensitivity is more exponential in character. The emissivity can be computed based on an optically thin plasma emission model such as CHIANTI (Young et al. 2003). Such calculations rely in turn on an assumed ion-equilibrium model. In the case of EUVI, EIT, and Atmospheric Imaging Assembly (AIA), the bands sensitive to coronal temperatures are dominated by Fe lines, greatly reducing the complexity of the abundance dependence. In those cases, the LDEM and the rms electron density (see below), will be inversely proportional to the assumed Fe abundance. Nevertheless, distinguishing abundance gradients from temperature gradients remains an issue. Ball et al. (2005) and García-Alvarez et al. (2006) considered DEM and abundances simultaneously in the context of stellar coronae.

Figure 2 shows the DEM kernel functions for the three Fe bands (171, 195, and 284 Å). The plots for the 304 Å band are not included, as its tomographic reconstructions have no simple quantitative interpretation, due to optical depth effects. The DEM kernel functions were computed as in Equation (22), using the bandpass functions $\phi_k(\lambda)$ shown in Figure 1, and computing the emissivity $N_{e0}^2 \psi(N_{e0}, \mathbf{a}_0, T; \lambda)$ with the CHIANTI model. As in Vázquez et al. (2009), we assumed a constant Fe abundance of $[\text{Fe}]/[\text{H}] = 1.26 \times 10^{-4}$ (Feldman et al. 1992), a low first ionization potential (FIP) element abundance enhanced by a factor of about 4 respect to typical photospheric values (Grevesse & Sauval 1998). We also assume for the Fe ions the results given by the ionization equilibrium calculations of Arnaud & Raymond (1992). The small differences between the bandpass functions for each band between the A and B spacecraft (see Figure 1) yield even smaller differences between the corresponding DEM kernel functions shown in Figure 2. This similarity is then what justifies the simultaneous use of data from both spacecraft to generate a common reconstruction for a given band.

Finally, Equation (21) can be inserted into Equation (15) to obtain the full forward problem

$$I_{k,j} = \sum_i w_{k,j,i} \int dT Q_k(T) \xi_i(T) + n_{k,j} \quad (24)$$

$$\approx \sum_i w_{k,j,i} \sum_l Q_{k,l} \xi_{i,l} + n_{k,j}, \quad (25)$$

where $Q_{k,l}$ and $\xi_{i,l}$ are representations of $Q_k(T)$ and $\xi_i(T)$ on a discrete temperature grid, i.e., the integral Equation (21) has been approximated with a sum.

5.1. LDEM Inverse Problem

Using Kronecker matrix products, Butala et al. (2008) showed how to represent Equation (25) in the standard matrix-vector form (i.e., with a single summation). However, treating the tomography step separately for each band is computationally convenient (FKW05) and the FBEs are useful products in their own right. The LDEM $\xi_i(T)$ can be estimated from the estimates of FBEs in voxel i determined from the tomographic step (e.g., Equation (20)). For example, in the case of EUVI, there are three FBE estimates (one for each of the 171, 195, and 284 Å bands), denoted as $\hat{\xi}_{0,i}$, $\hat{\xi}_{1,i}$, and $\hat{\xi}_{2,i}$. We define the vector $\hat{\xi}'_i \equiv \{\hat{\xi}_{k,i}, 1 \leq k \leq K\}$. Note that this vector contains only the FBE estimates in voxel i , in contrast to the vector ξ_k , which represents the FBEs in band k for all M voxels. The LDEM in voxel i be estimated by inverting Equation (21). Written in discrete form it becomes

$$\hat{\xi}'_i = \mathbf{Q} \xi_i + \mathbf{n}'_i, \quad (26)$$

where $\mathbf{Q} \equiv \{Q_{k,l}\}$, $\xi_i \equiv \{\xi_{i,l} \forall l\}$, and the statistics of \mathbf{n}'_i represent the uncertainty in $\hat{\xi}'_i$.

Pottasch (1963) seems to be the first to consider the problem of DEM inversion, and since then a wide variety of solutions have been proposed (e.g., Harrison & Thompson 1991; Landi & Landini 1997; FKW05; Prato et al. 2006). In the case of triple filter data such as that obtained from EUVI, TRACE, and EIT, the information is quite limited (Schmelz et al. 2007). However, it is enough to fit a Gaussian to the (L)DEM and to determine its three parameters (center, width, and area) via a best-fit criteria between the synthetic and the measured FBEs (Aschwanden et al. 2009; Vázquez et al. 2009). A new instrument called the AIA, to be launched on the Solar Dynamics Observatory (SDO), will have six Fe bands and dramatically improve the situation (Weber et al. 2004; FKW05).

The most complete description of the solution to the inversion of Equation (26) is given by Bayesian analysis in which a solution vector ξ_i is valued according to its *posterior probability*

$$P(\xi_i | \hat{\xi}'_i) = P(\xi_i) \frac{P(\hat{\xi}'_i | \xi_i)}{P(\hat{\xi}'_i)}, \quad (27)$$

where $P(\xi_i)$ is the assumed prior distribution, $P(\hat{\xi}'_i | \xi_i)$ is the likelihood (easily evaluated when \mathbf{n}'_i has Gaussian statistics), and $P(\hat{\xi}'_i)$ is a normalization factor (not a distribution since $\hat{\xi}'_i$ is fixed) to ensure that the posterior distribution integrates to unity. Kashyap & Drake (1998) and Schmelz et al. (2007) used a Markov chain Monte Carlo (Metropolis) algorithm to estimate posterior distributions in the DEM analysis of coronal plasma.

6. EXAMPLES

The data we analyzed consist of a 23.5 day time series of EUVI images from both the “ahead” (A) and “behind” (B) spacecraft, taken between 2008 April 16 and May 9, which is a time period corresponding to Carrington Rotation 2069. This is the same data set analyzed in Vázquez et al. (2009). During this time period, the A and B spacecraft were separated by a heliocentric angle of about 50°. This allowed 360° of view angles in 23.5 days, as opposed to 28 days as would be required for a single spacecraft. We took one image every 2 hr from the 171, 195, 284, and 304 Å bands (i.e., eight images in total every 2 hr) and, remarkably, there were no data gaps in either

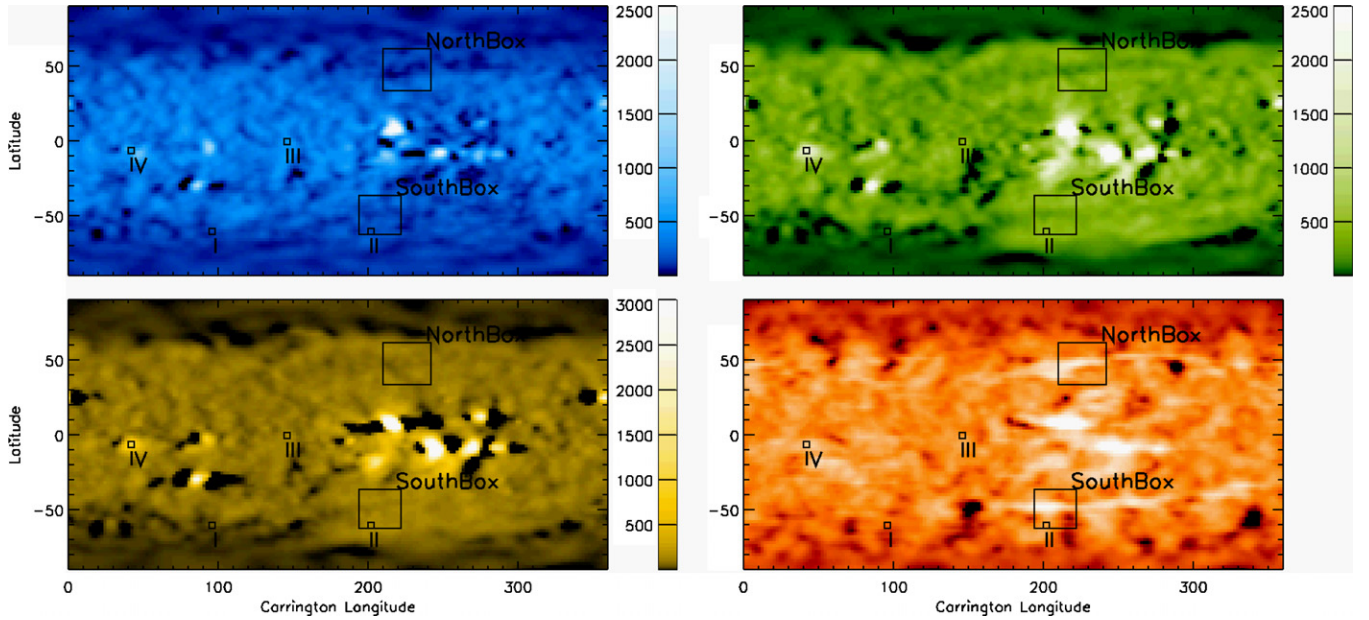


Figure 4. Maps of the (Carrington Rotation 2069) FBE ($\text{ph cm}^{-3} \text{sr}^{-1} \text{s}^{-1}$) reconstructions in the bands of 171 (top left), 195 (top right), and 284 Å (bottom left), at a height $r = 1.075 R_s$. Maps are thresholded for display. The 304 Å reconstruction (bottom right), shown at the height $r = 1.045 R_s$, was made using only above limb data. Due to optical depth effects, the 304 Å reconstruction does not have a straightforward quantitative interpretation, but it is useful for mapping filaments, two of which can be seen spanning (roughly) the longitudes between 200° and 300°. The properties of these filament cavities are the subject of the paper by Vásquez et al. (2009). The regions I, II, III, IV, NorthBox, and SouthBox, as discussed in the text (see also Figure 5), are indicated.

(A color version of this figure is available in the online journal.)

spacecraft or any band for the entire observation period (due to the high cadence, we used only about 5% of the available data).

Appendix A details all of the image preprocessing steps required to put the data in a final state appropriate to be used to perform the tomographic reconstructions. In particular, we computed time-binned images from the original ones. We divide each 24 hr period into four 6 hr bins. As we took images every 2 hr from the database, each binned image was the average of three original images. This average was performed pixel by pixel (see Appendix A), which greatly reduced the number of missing blocks (which were rare in the original images anyway). In Figure 3, the first column shows an example of such time-binned images from the EUVI-A instrument in the 171, 195, and 284 Å bands, taken around 20:00 UT on 2008 April 29. The second column is the corresponding synthetic images calculated by integrating the tomographic models along the LOS using Equation (12). In all cases, we show the logarithm of the intensity. The two columns use a common color scale for each band (row). The black streaks seen in the reconstructed images (specially in the 284 Å band) near some of the active regions (ARs) are ZDAs caused by the Sun’s temporal variability.

The computation grid is spherical with voxels that are regularly spaced in radius, latitude, and longitude (thus, the volume of the voxels increases as the radius squared) and it contains the entire volume between 1.0 and 1.26 R_s . The grid has 26 radial bins, 90 latitude bins, and 180 longitude bins, so each voxel is 0.01 R_s in height (7000 km) and is $2^\circ \times 2^\circ$ ($(2.44 \times 10^4 \text{ km})^2$ at the equator at 1.0 R_s). The reconstruction procedure assumed a static corona (i.e., we used Equation (20) instead of Equations (18), (19), and a Kalman filter).

Figure 4 shows reconstructed FBE ($\text{ph cm}^{-3} \text{sr}^{-1} \text{s}^{-1}$) maps of the 171, 195, and 284 Å bands, at a height of $r = 1.075 R_s$. A reconstruction of the emission in the 304 Å band at $r = 1.045 R_s$, is also displayed, but this serves only qualitative analysis purposes (e.g., mapping filaments) since optical depth

effects can be dominant in this band. This reconstruction was made only using the portion of the 304 Å band images above the limb (1.004 R_s). The boxed regions labeled I, II, III, and IV, each of which is 2 voxels by 2 voxels ($4^\circ \times 4^\circ$), indicate different types of coronal features. They were chosen within zones that exhibited very little temporal variability, as qualitatively (and subjectively) judged from the EUVI movies. These regions correspond to low-density subpolar “quiet Sun” (I), high-density subpolar “quiet Sun” (II), equatorial “quiet Sun” (III), and AR (IV, NOAA 0996).

For each of these regions, I through IV at $r = 1.075 R_s$, we averaged each band’s reconstructed FBE over the 4 voxels to obtain a value representative of each region. Using the three FBE values, we computed the LDEM in each region with the best-fit Gaussian criterion described in Section 5.1 to invert Equation (21). This procedure was also used by Vásquez et al. (2009), where it is explained in more detail. In Figure 5, we show the average LDEM for each region. The curves have different areas because they must integrate to the electron rms density (see Equation (23)), which is different for each one. The error bars in Figure 5 do not reflect the nonuniqueness inherent in inverting Equation (21) with limited information, rather they are derived from the intensities that are uncertain due to the range of acceptable values of the regularization parameter p (see the discussion after Equation (20)).⁴ The range of solutions depicted in the error bars in Figure 5 is derived from the best-fit Gaussians to the FBEs from the solutions with the optimal value of $p \pm$ (one standard deviation), and the error bars depict average uncertainties in the LDEM curves.

Figure 6 shows a map of the rms electron density at a height of $r = 1.075 R_s$. The average rms densities in regions I, II, III, and IV are $0.6\% \pm 5.5\%$, $0.9\% \pm 9.0\%$, $1.2\% \pm 1.5\%$, and $2.0\% \pm$

⁴ The range of values of the regularization parameter p is the standard deviation of its values derived from cross-validation trials (FJ02), adapted to the dual-spacecraft situation encountered here.

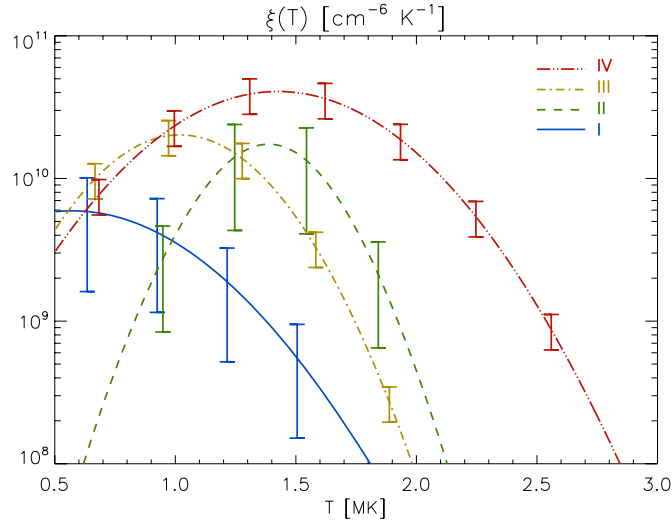


Figure 5. LDEM curves (assuming a Gaussian functional form) for regions I, II, III, and IV (at $1.075 R_s$) in Figure 4. Regions I and II are subpolar “quiet Sun,” of low and high density, respectively. Region III is equatorial “quiet Sun” and region IV is an AR.

(A color version of this figure is available in the online journal.)

$2.2\% \times 10^8 \text{ cm}^{-3}$, respectively. The uncertainty values are inherited from the error bars of the corresponding LDEM distributions. Since the emissivities in the EUVI bands (except 304 \AA) are dominated by Fe lines, the derived electron rms density value is inversely proportional to the assumed Fe abundance. In this work, we set the constant value $[\text{Fe}]/[\text{H}] = 1.26 \times 10^{-4}$ (Feldman et al. 1992), a low-FIP element abundance enhanced by a factor of about 4 with respect to typical photospheric values (Grevesse & Sauval 1998).

We selected two subpolar “quiet-Sun” regions (I and II). Inspecting the density map in Figures 5 and 6, it can be seen that the less dense region I exhibits a much cooler (referring to the center of the Gaussian curve) and broader temperature distribution than the denser region II. The LDEM distributions of the selected equatorial “quiet-Sun” region (III) and the AR (IV) also reveal very different plasmas, with the AR being much hotter and broader. This kind of LDEM is typical of the ARs we inspected. The particular AR reported here (NOAA 0996) has been chosen due to its isolation from other ARs and temporal stability, which is reflected by the lack of ZDAs, as explained in Section 4.1, that are present around most of the rest of the ARs.

6.1. 2D Versus 3D

Since the tomographic method presented here is limited to structures that are stable on the ≈ 2 week timescale, there is some debate as to the utility of our DENT method compared to standard DEM techniques. Clearly, for transient phenomena one must use only data taken within a short time span. In addition, DEM can be performed with high-resolution spectra containing many lines (e.g., Brosius et al. 1996), while having such spectral coverage in full-disk time series images for DENT would require a dedicated mission. These limitations notwithstanding, the value of 3D tomographic analysis is perhaps best illustrated through example.

For this purpose, we have revisited our already published 3D analysis of coronal cavities overlying polar crown filaments (Vázquez et al. 2009). In that paper, we analyzed two filament cavities, one located in the northern hemisphere and another one located in the southern hemisphere. In Figure 4, the regions analyzed are indicated as two boxes. The northern one (“NorthBox”) is centered at 226° and covers 32° in longitude, and the southern one (“SouthBox”) is centered at 208° and covers 28° in longitude. Both cavities are roughly east–west oriented, and can be readily seen in the images during their disk transits, as in the two left panels of Figure 7. This figure shows two boxes that lie inside NorthBox and SouthBox. The northern box is centered at 224° and the southern box at $210^\circ.5$, and both cover roughly 16° in longitude. Due to projection effects, it is impossible to make the boxes in the images match NorthBox and SouthBox exactly, except at a single height. We have opted to center the boxes on the projected centers of NorthBox and SouthBox assuming a height of $1.075 R_s$, and Figure 7 confirms that this choice corresponds to the cavity as seen in the images. Furthermore, the boxes cover about $1/2$ of the longitudinal extension of NorthBox and SouthBox, making the projection effects roughly homogeneous within each box. For these boxes, we analyzed the intensity along the north–south direction, averaged in the east–west direction. The right panel of Figure 7 shows an image for which CL $218^\circ.5$ lies roughly along the West limb, a longitude that is common to both boxes. Unlike the southern filament cavity, the northern filament cavity is never seen clearly on the limb (making it difficult to even identify the latitude of structure from the images alone) and hence no height information is available without tomographic analysis, which clearly shows the cavity is most pronounced around $1.075 R_s$. The southern filament cavity is sometimes clearly visible above the limb, so a specialized, model-based

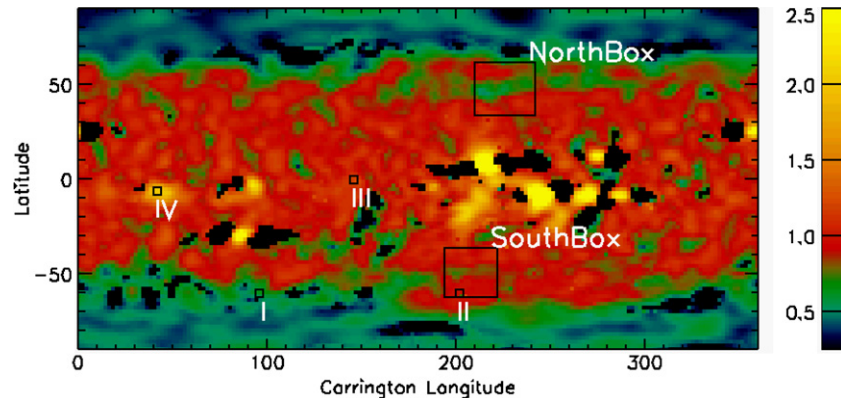


Figure 6. Map of the estimated electron density $(N_e^2)^{1/2}$ at a height $r = 1.075 R_s$, in units of 10^8 cm^{-3} . The color scale has been thresholded for display.

(A color version of this figure is available in the online journal.)

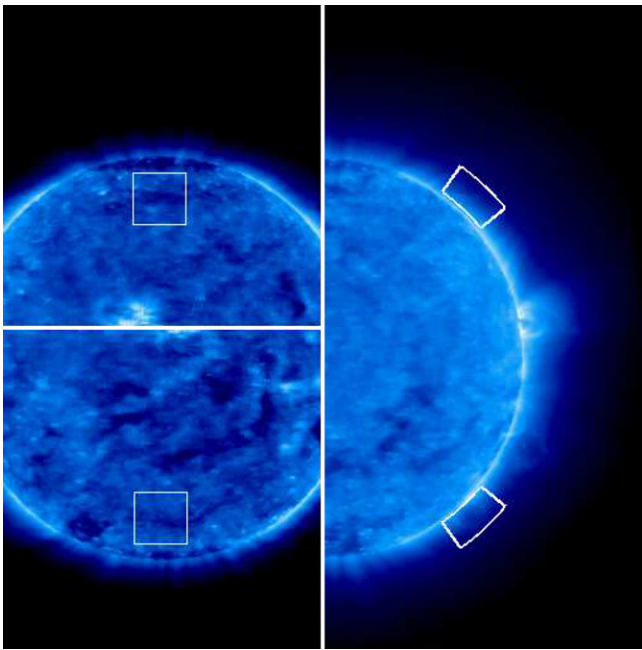


Figure 7. EUVI-A 171 Å images of the selected regions for study. Left panels: the northern and southern cavities during their disk transit. The northern selection is centered at 224° and the southern box at 210.5° and both cover roughly 16° in longitude. Right panel: longitude 218.5° lies roughly along the West limb, a longitude that is common to both selected cavity boxes. The upper left, lower left, and right images were taken in 2008 at 04.28.14:00, 04.29.14:00, and 05.05.20:00 UT, respectively.

(A color version of this figure is available in the online journal.)

3D analysis based on images is possible. For these reasons, it is hard to compare the north and south filament cavities from the images alone, however, our 3D tomographic analysis readily shows that these two filament cavities have essentially the same structure.

In order to simplify the analysis and see the structure as only a function latitude and height, we averaged the NorthBox and SouthBox reconstructions over all their longitude bins (32° and 28°, respectively). For the southern cavity, Figure 8 shows each band's reconstructed FBE as a function of latitude for several heights. Of particular interest is the fact that the 171 Å FBE (ζ_{171} , and similarly for the other bands) is greater than that of ζ_{195} at 1.035 R_s for all latitudes. At 1.055 R_s , ζ_{171} and ζ_{195} are comparable, and above that ζ_{195} is greater than ζ_{171} . Also, note that ζ_{284} remains well below ζ_{171} and ζ_{195} at all heights shown in the figure. Lending credibility to these results is that identical trends are seen for the northern cavity (results not shown here).

To make a direct comparison between the image intensities and these FBE results, we have averaged the intensities in the east–west direction for the two boxes indicated in the left panels of Figure 7. The resulting north–south average cuts for the southern box are shown in Figure 9. On the disk, the 171 Å band intensity (I_{171} , and similarly for the other bands) is greater than I_{195} at all latitudes. In Figure 10, we show the southern cavity intensity latitudinal dependence at several heights when longitude 218.5° was approximately on the limb. It can be seen that at 1.035 R_s , I_{171} and I_{195} are comparable and above that height I_{195} is greater at all latitudes. Our interpretation is that LOS integration, essentially height mixing, plays a significant role in all of the intensities seen in Figures 9 and 10, making the trend of the ratio ζ_{195}/ζ_{171} increasing with height much less clear in images than it is the tomographic reconstructions. A more serious LOS effect is seen at 1.075 and 1.095 R_s in

Figure 10, where I_{284} surpasses I_{171} in the core of the cavity (while no similar phenomenon is seen in the FBEs). This difference will dramatically alter the DEM results with respect to those from the LDEM analysis. We point out that the northern cavity had no clear presence above the limb and the intensity profiles there were useless for studying this structure, making a 3D analysis without tomographic methods difficult. The tomographic analysis of these filament cavities only required extracting the correct portion of the global solution. Without this tomographic analysis, interpreting the effects of LOS integration requires specialized modeling, perhaps along the lines of Fuller et al. (2008) for filaments.

7. SUMMARY AND DISCUSSION

We reviewed the quantitative theory of DENT and dealt with many practical aspects of its implementation. We presented the first EUV tomographic reconstructions of the Sun's corona, as well as the first multi-spacecraft tomographic reconstructions. We created 3D tomographic reconstructions of the EUVI 171, 195, and 284 Å band emissivities (FBEs) using data from both *STEREO* spacecraft taken for 23.5 days during Carrington rotation 2069 in 2008 April and May. To reduce the undesirable effects of optical depth on the tomographic reconstruction process, we ignored all the data in the images between projected radii of 0.98 and 1.025 R_s . This choice of rejection radii, indicated in Figure 3, was determined via the statistical test described in Appendix D. As a demonstration of the utility of the method and the relative ease of interpreting the results, we compared the tomographic reconstructions of the filament cavities studied in Vásquez et al. (2009) to intensity profiles from images of the structures both on the disk and above the limb. Our analysis shows that the LOS contamination is a significant or dominant effect for all of image intensities examined and that tomographic analysis leads easily and unambiguously to results without relying on ad hoc modeling procedures.

Figure 4 shows a spherical shell of the reconstructed emissivity (FBE) maps at a height of $r = 1.075 R_s$, for the four EUV bands. The 304 Å band reconstruction serves qualitative purposes due to optical depth effects. We also made a 3D reconstruction of the rms electron density N_e (cm^{-3}), a slice of which at the same height is shown in Figure 6. Figure 5 shows the LDEMs in the four distinct coronal regions, I through IV, that are indicated in Figure 3 and described in Section 6. The LDEM distributions (see Figure 5) were estimated under the assumption that they are Gaussian. While a Gaussian is a reasonable functional form to fit to most unimodal distributions, clearly it is not adequate for more complex distributions. Furthermore, the Gaussian fits shown here are just the minimum of a cost function, and there are other admissible solutions (including non-Gaussian ones) also within the uncertainties of the tomographic FBEs (which, in turn, are dominated by uncertainty in the regularization parameter p). In a later paper, we will use Markov chain Monte Carlo methods to find the set of admissible solutions (see Section 5). This will be especially useful with data from AIA's six Fe bands after SDO is launched. DEM inversion ambiguities notwithstanding, the following features stand out.

1. At the resolution of the tomographic analysis (the voxels are 7000 km in height and roughly $(2 \times 10^4 \text{ km})^2$ in basal area near the equator), the plasmas in the four selected regions are strongly nonisothermal (the Gaussian curve-fit is capable of recognizing an isothermal distribution). This

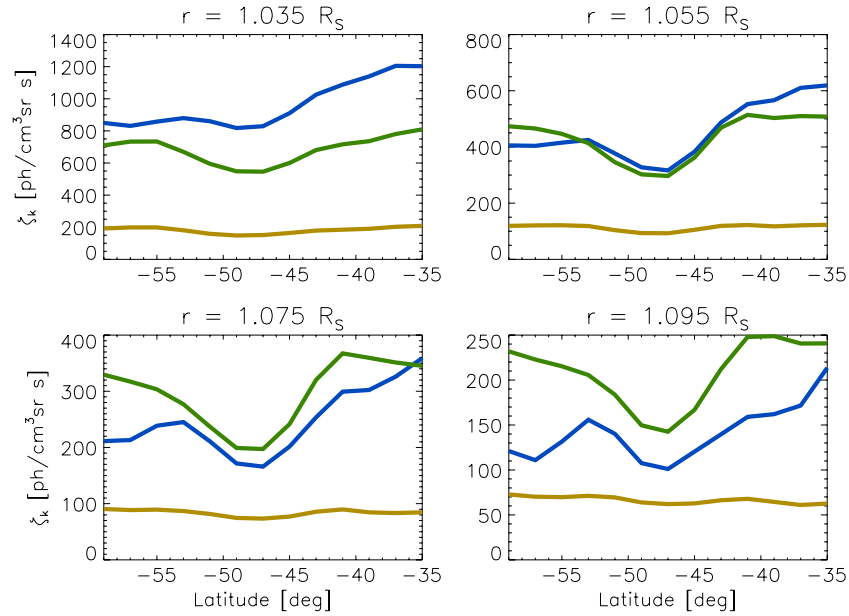


Figure 8. Longitude-averaged FBEs for SouthBox. The blue, green, and orange lines represent the 171, 195, and 284 Å bands, respectively. The NorthBox results are almost identical.

(A color version of this figure is available in the online journal.)

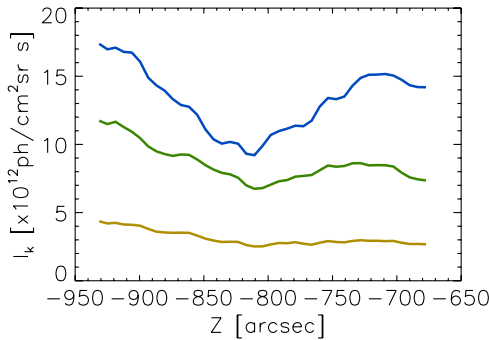


Figure 9. North-south intensity cuts for the southern box averaged in the east-west direction. See Figure 8 for colors.

(A color version of this figure is available in the online journal.)

means that flux tubes of differing temperatures are passing through the voxels.

2. Unlike previous DEM analyses, which were applied to images and had to make assumptions about foreground and background structures, this 3D tomographic analysis does not suffer from LOS confusion. Therefore, the conclusions drawn about temperature distributions cannot be ascribed such effects.
3. The 3D LDEM analysis here presented allows for the computation of estimated electron density N_e 3D maps down to very low heights. This complements the tomographic reconstructions based on white light coronagraph images, that usually cover much larger heights (e.g., Frazin et al. 2007; Vázquez et al 2008).

The main limitation of the DEMENT technique applied here is the assumption that the corona is static during the data acquisition period. The method is capable of resolving structures that are stable throughout their disk transits during the studied period, and the DEMENT results provide a kind of statistically averaged description, which could be advantageous for some types of analysis. The use of the twin EUVI A and B instruments,

and the extension of the tomographic technique to handle simultaneous multi-spacecraft data sets, has allowed us to gather the needed data in less time than a complete solar rotation. With the $\sim 50^\circ$ angular separation of the A and B *STEREO* spacecraft during the studied period, we decreased the data acquisition time by about 4 days. Comparison of the two columns in Figure 3 exemplifies how time-independent tomography can reproduce much of the Sun's observed structure. With the continuing separation of the *STEREO* spacecraft we plan to perform new global reconstructions in even less time in the near future, improving capabilities of the method. These methods will be enhanced by the application of Kalman filtering to create time-dependent tomographic reconstructions (Frazin et al. 2005a; Frazin & Kamalabadi 2005; Butala et al. 2008). Future work also will involve the analysis of different types of coronal structures, and coordinated coronal global modeling efforts (e.g., Vázquez et al. 2008). However, the full promise of DEMENT will not be realized until it is used to improve our understanding of how the Sun fills and heats the corona. Particularly desirable would be constraints on chromospheric processes, which are the origin of coronal structure.

We thank the anonymous referee for suggesting important improvements to this manuscript. We thank Jean-Pierre Wuelser for his invaluable assistance with the EUVI instrument and data. We thank Igor Sokolov for help with the level set formalism. This research was supported by NASA Heliophysics Guest Investigator award NNX08AJ09G to the University of Michigan, and the NSF SHINE and CMG programs, awards 0555561 and 0620550, respectively, to the University of Illinois. A.M.V. acknowledges the CONICET PIP/6220 and the ANPCyT PICT/33370-234 grants to IAFE for partial support.

The *STEREO*/SECCHI data used here are produced by an international consortium of the Naval Research Laboratory (USA), Lockheed Martin Solar and Astrophysics Lab (USA), NASA Goddard Space Flight Center (USA), Rutherford Appleton Laboratory (UK), University of Birmingham (UK),

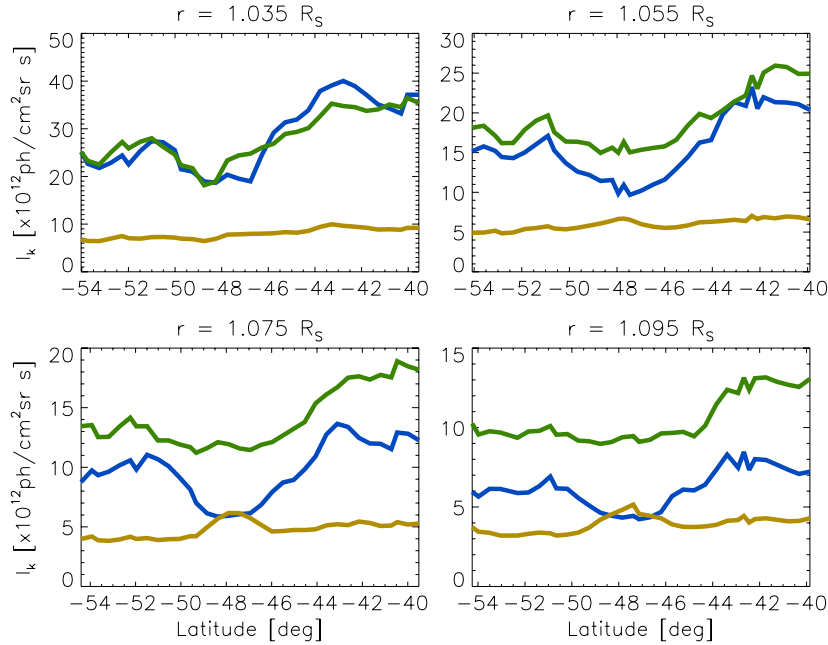


Figure 10. Off-limb, latitudinal intensity cuts for the southern box measured at longitude 218.5. See Figure 8 for colors.

(A color version of this figure is available in the online journal.)

Max-Planck-Institut für Sonnensystemforschung (Germany), Centre Spatiale de Liege (Belgium), Institut d'Optique Thorique et Appliquée (France), and Institut d'Astrophysique Spatiale (France).

APPENDIX A

IMAGE PREPROCESSING

To perform the EUV tomographic reconstructions presented here and in Vásquez et al. (2009), we selected one EUVI/STEREO (FITS format) image every 2 hr, for each band and spacecraft. The time interval spanned by the data must allow for 360° of coronal view angles, and depends on the spacecraft separation (it equals one solar rotational time for a single spacecraft, and less time using the two STEREO spacecraft). All selected images cover the full Sun and are of 2048² pixels in size. Here we describe the main aspects of data preprocessing required prior to performing the tomographic reconstructions.

The first step is the photometric calibration of the raw data and cleaning of cosmic ray hits. This can be accomplished using three IDL routines belonging to the *Solar Soft*⁵ SECCHI/STEREO software package, namely, `secchi_prep.pro`, `despike_gen.pro`, and `euvi_correction.pro`. First, `secchi_prep.pro` is used with flags set to calibrate the image into DN units, no exposure-time normalization or any other normalization is performed at this point. Specifically, the following flags are set: `/DN2P_OFF` (do not transform DN to PHOTONS), `/CALIMG_OFF` (do not flatfield, as is recommended as of article submission; J.-P. Wuelser 2008, private communication), `/NORMAL_OFF` (do not normalize intensities to OPEN filter position), and `/EXPTIME_OFF` (do not normalize by exposure time). Then, `despike_gen.pro` is used to clean the image of cosmic ray hits. This routine implements a selective median filter: if the difference between each image pixel and its 3 × 3 neighbors median exceeds a given threshold, then that image pixel is replaced by another value. The threshold used to evaluate this

decision is controlled by the value of a variable TN that can be set by the user. Based on our experience, and guidance from the EUVI team, we set TN=8 for the 171 and 195 Å bands, and TN=4 for the 284 Å band. Also, we have used the `/low3` flag, which picks as replacement value the third lowest value of the 3 × 3 pixel neighborhood (while the usual 3 × 3 median filter would pick the fifth lowest). This feature, along with running of `despike_gen.pro` repeatedly, proves to be efficient when cosmic ray hits cause pixel bleeding, as well as in the removal of artifacts significantly larger than one pixel. Typically, more than 99% of the pixels remain unchanged after the despiking filter is applied. Finally, the `euvi_correction.pro` is used to perform the tasks needed to complete the calibration, setting the flags `/DN2P_OFF`, `/CALIMG_OFF`, and `/NORMAL_OFF` (same as explained above). All the above steps generate final images in units of (dn/s). We have also generated images in units of (PHOTONS) for statistical studies. The process to achieve this is the same as explained above, but canceling the flag `/DN2P_OFF` and setting the flag `/EXPTIME_OFF` when using the `euvi_correction.pro` routine in the last step. The dn/s calibrated images go through further preprocessing, specifically oriented to the tomographic reconstruction. In the following list, we itemize its most important aspects.

1. We pixel-rebin the images, for consistency with the grid size set for the reconstruction and to decrease the memory requirements. The EUVI images are originally 2048² pixels in size, and in our previous papers we currently rebin the images down to 1024² pixels, decreasing their size by a factor of 4 (in turn, the tomography code adds four LOS sums, corresponding to 2 × 2 bins of the 1024² images, together for further reduction).
2. We rotate the images to align the north pole up. Strictly, this is not required by the tomographic code, as it properly identifies the image orientation from its header information, but it proves to be useful for producing movies of the data time series, for both inspection and display purposes.
3. We apply to the images the correction factors α_k and the renormalization factors $\Phi_{k,0}$, as in Equation (B2).

⁵ <http://www.lmsal.com/solarsoft/>

4. Using the FITS file header information, during all this preprocessing the pixels that belong to missing blocks are properly identified. A key value “-999.0” is assigned to those pixels for their posterior rejection by the tomographic code.
5. Finally, we compute time-binned images out of the original ones. Currently, we divide each 24 hr period into four bins of 6 hr, so that each binned image is an average of three original ones. Specifically, each pixel in the binned image is the average of the corresponding pixel in the original images, excluding any pixels that belong to blocks of missing data. As missing blocks are unlikely to occur in the same location of the detector in two different images, this time-binning greatly reduces the number of missing blocks in the binned images (that were very rare in the original images already).
6. All the relevant FITS file header information is modified to properly document all steps mentioned above.

After applying these tasks to a time series of images allowing for 360° of coronal view angles, a set of images suitable to perform a tomographic reconstruction is obtained.

APPENDIX B

MULTI-SPACECRAFT FORMULATION

In this era of the dual-spacecraft *STEREO* mission, we have the opportunity to combine simultaneous observations of the corona from multiple viewpoints. This combination of multi-instrument data is only useful for our purposes if the individual temperature response functions $Q_k(T)$, derived from the band-pass functions $\phi_k(\lambda)$, are similar enough for the *STEREO* A and B spacecraft. Otherwise the measurements from different instruments would weigh the plasma temperature distribution differently. Figure 1 shows laboratory measurements of the bandpass functions for all four bands of the EUVI/*STEREO* instruments. As can be seen, for each band the differences between the two spacecraft curves are small. The largest discrepancy is observed around the peak of the 171 Å band, but even that discrepancy implies a quite negligible difference in the corresponding DEM kernel function Q_{171} (see Section 5), as shown in Figure 2. Since the measurements show that the EUVI instruments on the *STEREO* A and B spacecraft have very similar bandpasses, and we ignore the small differences both here and in Vásquez et al. (2009).

Our analysis of in-flight data shows that the two instrument calibrations exhibit a small-scale difference (which manifests as the $\Phi_{k,0}$ factor in Equation (7)) that must be resolved before combining their data in the tomographic inversion. Detailed comparisons of measurements from EUVI A and B were made in 2007 January, just after launch, when the two spacecraft were close to the Earth and separated by much less than 1° in heliocentric angle. Because the separation was so small, they were seeing almost exactly the same face of the Sun. These data show that the measured intensities (which have been processed from the raw data in accordance with Appendix A) in the 171, 195, and 284 Å bands in the EUVI A instrument are several percent lower than those in EUVI B. We used those data to compute the correction factors (α_k) required to bring the A and B intensities into agreement. The following variant of Equation (17) defines the dual spacecraft tomographic inversion problem, taking correction factors into account (see the change

Table 1

The EUVI Calibration Values (as of the 2008 February 19) of the Normalization Constants $\Phi_{k,0}/\Omega_p$ (dn cm²/ph) for the *STEREO* A and B Spacecraft, Each Bandpass (“open” filter), and the Values of Associated α_k (dimensionless) Required to Reconcile Intensity Differences Observed in 2007 January (see Appendix B)

Band	$\Phi_{k,0}^A/\Omega_p$	$\Phi_{k,0}^B/\Omega_p$	α_k^A	α_k^B
171	2.833×10^{-1}	2.430×10^{-1}	1.027	0.975
195	1.420×10^{-1}	1.230×10^{-1}	1.038	0.965
284	2.827×10^{-2}	2.491×10^{-2}	1.051	0.953
304	4.242×10^{-2}	4.435×10^{-2}		

Notes. We did not calculate the α_k values for the 304 Å band since we did not use those images for quantitative purposes.

of variables after Equation (15))

$$\begin{bmatrix} \alpha_k^A \mathbf{I}_k^A / \Phi_{k,0}^A \\ \alpha_k^B \mathbf{I}_k^B / \Phi_{k,0}^B \end{bmatrix} = \begin{bmatrix} \mathbf{W}_k^A \\ \mathbf{W}_k^B \end{bmatrix} \boldsymbol{\zeta}_k + \begin{bmatrix} \alpha_k^A \mathbf{n}_k^A / \Phi_{k,0}^A \\ \alpha_k^B \mathbf{n}_k^B / \Phi_{k,0}^B \end{bmatrix}, \quad (\text{B1})$$

where α_k^A and α_k^B are the correction factors, and \mathbf{I}_k^A and \mathbf{I}_k^B are the measured intensities from A and B, respectively. If the different values of $\Phi_{k,0}$ for A and B explained any observed intensity differences, the α_k^A and α_k^B correction factors would not be necessary. In Table 1, we show the numerical values of these factors, for both spacecraft and all bands.

Finally, we define several aggregate vectors and matrices in order to unify the notation:

$$\begin{bmatrix} \alpha_k^A \mathbf{I}_k^A / \Phi_{k,0}^A \\ \alpha_k^B \mathbf{I}_k^B / \Phi_{k,0}^B \end{bmatrix} \rightarrow \mathbf{I}_k \quad (\text{B2})$$

$$\begin{bmatrix} \mathbf{W}_k^A \\ \mathbf{W}_k^B \end{bmatrix} \rightarrow \mathbf{W}_k \quad (\text{B3})$$

$$\begin{bmatrix} \alpha_k^A \mathbf{n}_k^A / \Phi_{k,0}^A \\ \alpha_k^B \mathbf{n}_k^B / \Phi_{k,0}^B \end{bmatrix} \rightarrow \mathbf{n}_k. \quad (\text{B4})$$

With these definitions, Equation (B1) can be rewritten as Equation (17). Of course, generalization to three or more spacecraft is straightforward.

APPENDIX C

LEVEL-SET FORMALISM AND THE LDEM

The goal of this appendix is the derivation of Equation (21), which relates the LDEM to the FBE, and to show that the mean-square density can be obtained by integrating the LDEM. A similar equation that relates the DEM to intensity of a spectral line or an image point can be found, e.g., in Brown et al. (1991). While most derivations of relationship of the DEM to the intensity involve complicated integrals over isothermal surfaces, our development uses levels sets and is more straightforward. This appears to be the first use of the level set formalism for this application. Essentially, the same methodology can be used to relate intensity measurements to the DEM.

Equation (14) defines $\zeta_k(\mathbf{r})$, the FBE in the k th band at a given point in the corona \mathbf{r} , however, the tomographic inversion assumes a discrete corona in which the FBE is assumed to

be constant in the interior volume of each voxel. Let \mathcal{R}_i be the (closed) set of points defining the volume of the i th voxel. Equation (15) is the inverse problem from which the $\zeta_{k,i}$, the FBE for the k th band i th voxel, can be determined. We take $\zeta_{k,i}$ to be the volume average of $\zeta_k(\mathbf{r})$ in the i th voxel, i.e.,

$$\zeta_{k,i} \equiv \frac{1}{V_i} \int_{\mathcal{R}_i} d^3\mathbf{r} \zeta_k(\mathbf{r}), \quad (\text{C1})$$

where V_i is the volume of the i th voxel. Using Equation (14), Equation (C1) becomes

$$\zeta_{k,i} \equiv \frac{1}{V_i} \int_{\mathcal{R}_i} d^3\mathbf{r} N_e^2(\mathbf{r}) Q_k(T(\mathbf{r})), \quad (\text{C2})$$

where, as in Equation (22), $Q_k(\mathbf{r}) \equiv \int d\lambda \phi_k(\lambda) \psi(N_{e0}, \mathbf{a}_0, T(\mathbf{r}))$, in which N_{e0} and \mathbf{a}_0 , are fixed, appropriate values of the electron density (which is not critical here since most of the dependence on it has been factored out, as described in Section 5) and the elemental abundances.

The set of points $L(T_0)$ defined as

$$L(T_0) \equiv \{\mathbf{r} : T(\mathbf{r}) = T_0 \text{ and } \mathbf{r} \in \mathcal{R}_i\} \quad (\text{C3})$$

specifies a set of points within \mathcal{R}_i and is known as a *level set*. The sets L and Λ (see below) should have voxel subscripts, since they only pertain to points within the i th voxel, but we drop this notation for convenience. Since there is no finite volume of plasma with a temperature of exactly T_0 (i.e., there is no open set satisfying Equation (C3)), $L(T_0)$ has measure 0. Now consider a (closed) set of points composed of a family of level sets

$$\Lambda(T_0, \Delta T) \equiv \{\mathbf{r} : T_0 \leq T(\mathbf{r}) \leq T_0 + \Delta T, \mathbf{r} \in \mathcal{R}_i\}. \quad (\text{C4})$$

Because $T(\mathbf{r})$ is piecewise continuous, for finite ΔT , if any of the plasma falls within the range $(T_0, T_0 + \Delta T)$, $\Lambda(T_0, \Delta T)$ will have nonzero measure (volume). In the limit $\Delta T \rightarrow 0$ the measure is

$$d\{\Lambda(T, dT)\} = \frac{(dT)^3}{|\partial T/\partial x_1| |\partial T/\partial x_2| |\partial T/\partial x_3|} = d^3\mathbf{r}, \quad (\text{C5})$$

where $\mathbf{r} = (x_1, x_2, x_3)$, and the derivatives are evaluated at the location \mathbf{r}_0 (which satisfies $T(\mathbf{r}_0) = T_0$). If there is more than one location at which $T(\mathbf{r}) = T_0$, the measures need to be added. Since all of the points in the volume \mathcal{R}_i are at some temperature between 0 and ∞ , V_i must satisfy

$$\int_0^\infty dT d\{\Lambda(T, dT)\}/dT = \int_{\mathcal{R}_i} d^3\mathbf{r} = V_i. \quad (\text{C6})$$

Next, we define an indicator function

$$H_{\Lambda(T, \Delta T)}(\mathbf{r}) \equiv \begin{cases} 1/\Delta T & \text{if } \mathbf{r} \in \Lambda(T, \Delta T) \\ 0 & \text{if } \mathbf{r} \notin \Lambda(T, \Delta T) \end{cases}, \quad (\text{C7})$$

which has units of (K^{-1}) and satisfies

$$\int_0^\infty dT H_{\Lambda(T, dT)}(\mathbf{r}) = 1, \quad (\text{C8})$$

meaning that the plasma at any given location is at one temperature. Integrating Equation (C8) over the voxel volume, the condition given by Equation (C6) can be rewritten as the double integral

$$\int_{\mathcal{R}_i} d^3\mathbf{r} = \int_0^\infty dT \int_{\mathcal{R}_i} d^3\mathbf{r} H_{\Lambda(T, dT)}(\mathbf{r}). \quad (\text{C9})$$

Similarly, the voxel-volume integral of any function $f(\mathbf{r})$ will satisfy the condition

$$\int_{\mathcal{R}_i} d^3\mathbf{r} f(\mathbf{r}) = \int_0^\infty dT \int_{\mathcal{R}_i} d^3\mathbf{r} f(\mathbf{r}) H_{\Lambda(T, dT)}(\mathbf{r}). \quad (\text{C10})$$

The LDEM, which has units $(\text{cm}^{-6} \text{ K}^{-1})$, can now be defined as

$$\xi_i(T) \equiv \frac{1}{V_i} \int_{\mathcal{R}_i} d^3\mathbf{r} N_e^2(\mathbf{r}) H_{\Lambda(T, dT)}(\mathbf{r}), \quad (\text{C11})$$

meaning that $\xi_i(T)$ is the voxel-volume integral of N_e^2 , but the integral is only taken over the volume in which the plasma has a temperature between T and $T + dT$. We can now use Equations (C10) and (C11) to rewrite the integral in Equation (C2) as

$$\zeta_{k,i} \equiv \frac{1}{V_i} \int_{\mathcal{R}_i} d^3\mathbf{r} N_e^2(\mathbf{r}) Q_k(T(\mathbf{r})) \quad (\text{C12})$$

$$= \frac{1}{V_i} \int_0^\infty dT \int_{\mathcal{R}_i} d^3\mathbf{r} N_e^2(\mathbf{r}) Q_k(T(\mathbf{r})) H_{\Lambda(T, dT)}(\mathbf{r}) \quad (\text{C13})$$

$$= \frac{1}{V_i} \int_0^\infty dT Q_k(T) \int_{\mathcal{R}_i} d^3\mathbf{r} N_e^2(\mathbf{r}) H_{\Lambda(T, dT)}(\mathbf{r}) \quad (\text{C14})$$

$$= \int_0^\infty dT Q_k(T) \xi_i(T), \quad (\text{C15})$$

where $Q_k(T(\mathbf{r}))$ factors out of the interior integral in Equation (C13), because the temperature is constant where the indicator function is nonzero. Thus, Equation (21) is proved.

The local emission measure (LEM), which has units (cm^{-6}) , is the mean-square density and can (in principle) be determined by integrating the LDEM as follows:

$$\mu_i \equiv \frac{1}{V_i} \int_{\mathcal{R}_i} d^3\mathbf{r} N_e^2(\mathbf{r}) \quad (\text{C16})$$

$$= \frac{1}{V_i} \int_0^\infty dT \int_{\mathcal{R}_i} d^3\mathbf{r} H_{\Lambda(T, dT)}(\mathbf{r}) N_e^2(\mathbf{r}) \quad (\text{C17})$$

$$= \int_0^\infty dT \xi_i(T). \quad (\text{C18})$$

The rms electron density (in cm^{-3} units) at each voxel can be determined via

$$\langle N_e^2 \rangle_i^{1/2} \equiv \sqrt{\mu_i} \quad (\text{C19})$$

Essentially identical arguments can be applied in standard DEM analysis to the relationship between the intensity and the DEM. The only difference is that line integrals are used instead of volume integrals, and the other quantities must be defined accordingly.

APPENDIX D

THE χ^2 TEST FOR DATA REJECTION

The effects of optical depth on the tomographic reconstruction can be mitigated by rejecting the EUVI image pixels corresponding to the most optically thick part of the image. The data to be rejected are located between projected radii r_i and r_o , chosen to be slightly less than and greater than $1.0 R_s$, respectively. Of the three EUVI Fe bands, the 171 Å band is the most susceptible to optical depth effects due to the oscillator strength and maximum ion fraction of the Fe X 171.08 Å line, which are much greater than those of the Fe XII 195.12 and Fe XV 284.15 Å

Table 2
Table of r_i and r_o , and the Associated χ_r^2 Values for the 171 Å Band Reconstruction

r_i (R_s)	r_o (R_s)	χ_r^2
0.97	1.09	30.6
0.97	1.045	31.7
0.98	1.045	32.2
0.98	1.025	36.9
0.99	1.065	32.9
0.99	1.025	39.1
...	...	106

lines dominating the other two bands (e.g., Schrijver et al. 1994). In Vásquez et al. (2009), as well here, we choose the values of r_i and r_o with the χ^2 test described in this appendix.

For this purpose, the reduced χ^2 statistic (χ_r^2), which is a measure of “goodness-of-fit,” is defined as

$$\chi_r^2 \equiv \frac{1}{N - P} \sum_{k=1}^N \frac{(\hat{y}_k - y_k)^2}{\sigma_k^2}, \quad (\text{D1})$$

where $\{y_k, k = 1, \dots, N\}$ are the data points to be fitted by $\{\hat{y}_k, k = 1, \dots, N\}$, which are linear functions of a vector with P elements, and σ_k are the standard deviations of the data points (assumed to be statistically independent) due to noise. Of course, we require $0 < P < N$. For example, consider least-squares fitting a polynomial of degree $P - 1$ to N data points $\{y_k\}$ (located, say, at the first N integers along the real line) with normally distributed with variances $\{\sigma_k^2\}$. The vector with P elements contains the values of the polynomial coefficients to be determined via the weighted least-squares fitting procedure, and $\{\hat{y}_k\}$ are the values of the fitted polynomial. Then, for the expectation we have $\langle \chi_r^2 \rangle = 1$.

In this case, $\{y_k\}$ are pixel intensity values from the EUVI images used as input for a tomographic reconstruction, $\{\sigma_k\}$ are given by Poisson photon statistics, and P is the number of voxels in the reconstruction (for the $13 \times 60 \times 120$ grid, $P = 93, 600$). The functions \hat{y}_k are the synthetic intensity values determined from LOS integration of the tomographic reconstruction, as in Equation (12) and shown in the right column of Figure 3. The value of N depends on the amount of data that is rejected (i.e., r_i and r_o), but for no data rejection and the EUVI images binned down to 256×256 , the value was about 3.3×10^6 . Table 2 gives the χ_r^2 value for various values r_i and r_o . The last line corresponds to no data rejection. We have assumed that rejecting all of the data between 0.97 and 1.09 R_s removes most of the optically thick LOSs and represents something close to the minimum value that could be achieved in this way. As the table shows, the value of χ_r^2 for these rejection radii is 30.6. The fact that χ_r^2 never approaches unity is most likely due to the small amount of Poisson noise (large number of counts) and the effects of the corona’s temporal variability. Note that in the case of no data rejection the value of χ_r^2 is much greater (106) and that any of chosen values of r_i and r_o in the table give a vast improvement. We chose the values of 0.98 and 1.025 R_s because it seemed to be a reasonable compromise between having more usable bottom layers in the reconstruction (the layers below r_o were not usable) and a lower χ_r^2 value. Very similar trends were seen in the 195 and 284 Å bands, but reduction in the value of χ_r^2 caused by the data rejection were much less dramatic due to the lesser importance of optical depth effects in these bands.

APPENDIX E

LINE-OF-SIGHT GEOMETRY

The specific intensity measured by pixel j , $J_j(\lambda)$, is given by an LOS integral through the corona (Equation (9)). Tomographic reconstruction requires specification of the locus of points that define this LOS so that one can determine the volume elements of the computation grid that the LOS passes through and the path length through each such element (see the \mathbf{W}_k matrix in Equation (16)). In order to do this calculation, one must determine the equation of the LOS in the appropriate reference frame, i.e., a frame rotates with the Sun. The discussion in this appendix is similar to that presented by FJ02 in the context of white-light tomography, but has several additions. The present discussion also corrects an error (Equation (10) of FJ02, and Equation (E2) here) which had no practical consequences for the reconstructions previously published by Frazin and colleagues.

We will refer to three coordinate systems, numbered 1, 2, and 3. All three coordinate systems are right handed and heliocentric. \mathbf{e}_x , \mathbf{e}_y , and \mathbf{e}_z are the unit vectors associated with the coordinate axes. The symbols \mathbf{o} , $\hat{\mathbf{p}}$, \mathbf{q} , and $\hat{\mathbf{l}}$ represent the origin-observer vector, the solar pole unit vector, the point of closest approach to the Sun (the *near point*) of the LOS, and the unit vector parallel to the LOS, respectively. \mathbf{o} , $\hat{\mathbf{p}}$, \mathbf{q} , $\hat{\mathbf{l}}$, \mathbf{e}_x , \mathbf{e}_y , and \mathbf{e}_z are column vectors with three elements. The numerical subscript on any vector denotes the coordinate system to which it belongs; for example, $\hat{\mathbf{p}}_2$ is the solar pole unit vector in the second coordinate system. \mathbf{R}_{12} and \mathbf{R}_{23} are the matrices which transform vectors from coordinate system 1 to 2 and 2 to 3, respectively. $\mathbf{R}_x(\vartheta)$, $\mathbf{R}_y(\vartheta)$, and $\mathbf{R}_z(\vartheta)$ represent the standard matrices for counterclockwise rotation through an angle ϑ about the x , y , and z axes, respectively.⁶

In the coordinate system specified by index v ($v = 1, 2$, or 3), the locus of points along the LOS corresponding to image pixel j is given by the expression

$$\mathbf{r}_j(l) = \mathbf{q}_{j,v} + \hat{\mathbf{l}}_{j,v} l, \quad l_{\min,j} < l < l_{\max,j}, \quad (\text{E1})$$

where $l_{\min,j}$ and $l_{\max,j}$ are where the LOS enters and exits the computation grid, respectively. Note that $\mathbf{q}_{j,v}$ and $\hat{\mathbf{l}}_{j,v}$ are perpendicular, so their inner product $\mathbf{q}_{j,v}^T \hat{\mathbf{l}}_{j,v} = 0$ (the superscript T indicates transpose). The goal of this appendix is to show how $\mathbf{q}_{j,3}$ and $\hat{\mathbf{l}}_{j,3}$ are calculated.

The three coordinate systems and the associated vectors and transformation matrices are as follows.

1. The first coordinate system, called heliocentric inertial (HCI) coordinates, differs from geocentric inertial coordinates (GCI) only by the choice of origin. The GCI coordinate system is closely related to the J2000 Earth equatorial coordinate system, which is the standard system of celestial coordinates in which the right ascension and declination of objects are specified.⁷ This coordinate system is useful because the solar pole unit vector $\hat{\mathbf{p}}_1$ is known a priori (the J2000 right ascension and declination of the solar pole are approximately $286^\circ 11'$ and $+63^\circ 85'$, respectively).

⁶ For example, $\mathbf{R}_x(\vartheta) = \begin{bmatrix} 1 & 0 & 0 \\ 0 & \cos \vartheta & -\sin \vartheta \\ 0 & \sin \vartheta & \cos \vartheta \end{bmatrix}$, with the same ordering for \mathbf{R}_y and \mathbf{R}_z .

⁷ If α and δ are the J2000 right ascension and declination of an object, then the associated unit vector (GCI coordinates) pointing to it is $[\cos \delta \cos \alpha, \cos \delta \sin \alpha, \sin \delta]^T$.

For *SOHO* data, there are orbit files that contain the GCI Earth–Sun vector and the GCI Earth–*SOHO* vector, from which one may determine the HCI Sun–observer vector \mathbf{o}_1 . In the case of *STEREO*, the FITS files (which contain the images) give the spacecraft coordinates in heliocentric Aries ecliptic (HAE) coordinates. The HAE to HCI coordinate transformation matrix is $\mathbf{R}_x(\varphi)$, where φ is the J2000 obliquity of the ecliptic $23^\circ 26' 21''.4119$ (Allen 1976).

- The second coordinate system is convenient for calculating the LOS associated with each pixel in the images. In this system, the x -axis is coincident with the origin–observer vector, so $\mathbf{e}_{x2} = \mathbf{o}_2 / \|\mathbf{o}_2\| = \mathbf{R}_{12}\mathbf{o}_1 / \|\mathbf{o}_1\|$ (length invariance under rotation implies $\|\mathbf{o}_2\| = \|\mathbf{o}_1\|$). As images are often displayed with the north pole at the top, it is convenient to set the y -component of the solar pole unit vector to 0; thus, $\hat{\mathbf{p}}_2 = \mathbf{R}_{12}\hat{\mathbf{p}}_1 = [\sin\chi, 0, \cos\chi]^T$, where χ is the tilt-angle of the solar pole with respect to the plane of the sky (the so-called “ B angle”). These conditions are sufficient to specify \mathbf{R}_{12} . We have $\mathbf{R}_{12} = \mathbf{R}_x(c)\mathbf{R}_y(b)\mathbf{R}_z(a)$, in which $\mathbf{R}_z(a)$ zeros the y -component of \mathbf{o}_1 , $\mathbf{R}_y(b)$ zeros the z -component of $\mathbf{R}_z(a)\mathbf{o}_1$, and $\mathbf{R}_x(c)$ zeros the y -component of $\mathbf{R}_y(b)\mathbf{R}_z(a)\hat{\mathbf{p}}_1$. The near point vector is given by⁸

$$\mathbf{q}_{j,2} = d \mathbf{R}_x(\eta_j) [\sin \rho_j \tan \rho_j, 0, \sin \rho_j]^T, \quad (\text{E2})$$

where d is the origin–observer distance, and η_j and ρ_j are the position angle (measured counterclockwise from north in the image) and projected radius (in radians) of the image pixel j , respectively. Similarly, the unit vector in the LOS direction is given by

$$\hat{\mathbf{l}}_{j,2} = \mathbf{R}_x(\eta_j) [-\cos \rho_j, 0, \sin \rho_j]^T. \quad (\text{E3})$$

- The third coordinate system, also known as Carrington heliographic coordinates (Thompson 2006), rotates with the Sun and is the domain in which the tomographic computation grid is defined. In this coordinate system, the z -axis is parallel to the solar pole unit vector, so $\mathbf{e}_{z3} = \hat{\mathbf{p}}_3 = \mathbf{R}_{23}\mathbf{R}_{12}\hat{\mathbf{p}}_1$. The vectors \mathbf{e}_{x3} and \mathbf{e}_{y3} therefore span the equatorial plane, and we take \mathbf{e}_{x3} to point toward the meridian of 0° Carrington longitude. \mathbf{e}_{y3} is chosen to complete a right-handed coordinate system, so it points toward the meridian of 90° Carrington longitude. The above conditions are enough to specify \mathbf{R}_{23} . Thus, $\mathbf{R}_{23} = \mathbf{R}_z(-\psi)\mathbf{R}_y(\chi)$, where χ is the polar tilt angle given above and ψ is the Carrington longitude of the observer. $\mathbf{R}_y(\chi)$ zeros the x -component of $\hat{\mathbf{p}}_2$ and $\mathbf{R}_z(\psi)$ accounts for the solar rotation. While the *STEREO* FITS files contain the value of ψ , in the case of *SOHO*, the angle ψ can be calculated as described in FJ02.

Note that while d , ψ , and χ are constant within each image, they change from one image to the next as the observer moves and the Sun rotates.

The locus of points along the LOS in the third coordinate system is given by Equation (E1), with $\hat{\mathbf{l}}_{j,3} = \mathbf{R}_{23}\hat{\mathbf{l}}_{j,2}$ and $\mathbf{q}_{j,3} = \mathbf{R}_{23}\mathbf{q}_{j,2}$, using Equations (E2) and (E3). The length

of this LOS though a given volume element of the computation grid (compared to Equation (16)) can now be calculated with straightforward trigonometric computations once the grid structure has been defined.

REFERENCES

- Allen, C. W. 1976, *Astrophysical Quantities* (London: Athlone)
- Arnaud, M., & Raymond, J. C. 1992, *ApJ*, **398**, 39
- Aschwanden, M. J., Wuelser, J. P., Nitta, N. V., Lemen, J. R., & Sandman, A. 2009, *ApJ*, **695**, 12
- Ball, B., et al. 2005, *ApJ*, **634**, 1336
- Born, M., & Wolf, E. 1999, *Principles of Optics* (7th expanded ed.; Cambridge: Cambridge Univ. Press)
- Brosius, J. W., Davila, J. M., Thomas, R. J., & Monsignori-Fossi, B. C. 1996, *ApJS*, **106**, 143
- Brown, J. C., Dwivedi, B. N., Sweet, P. A., & Almléaky, Y. M. 1991, *A&A*, **249**, 277
- Butala, M. D., Kamalabadi, F., Frazin, R. A., & Chen, Y. 2008, *IEEE J. Sel. Top. Signal Process.*, **2**, 75
- Butala, M. D., Kamalabadi, F., Frazin, R. A., & Chen, Y. 2009, *IEEE Trans. Signal Process.*, **18**, 1573
- Daley, R. 1991, *Atmospheric Data Analysis* (Cambridge: Cambridge Univ. Press)
- DeForest, C. E., Martens, P. C. H., & Wills-Davey, M. J. 2009, *ApJ*, **690**, 1264
- Demoment, G. 1989, *IEEE Trans. Acoustics, Speech, Signal Proc.*, **37**(12), 2024
- Evensen, G. 2007, *Data Assimilation: The Ensemble Kalman Filter* (Berlin: Springer)
- Feldman, U., Mandelbaum, P., Seely, J. L., Doschek, G. A., & Gursky, H. 1992, *ApJS*, **81**, 387
- Frazin, R. A., Butala, M. D., Kemball, A., & Kamalabadi, F. 2005a, *ApJ*, **635**, L197
- Frazin, R. A. 2000, *ApJ*, **530**, 1026
- Frazin, R. A., & Janzen, P. 2002, *ApJ*, **570**, 408 (FJ02)
- Frazin, R. A., & Kamalabadi, F. 2005, *Sol. Phys.*, **228**, 219
- Frazin, R. A., Kamalabadi, F., & Weber, M. A. 2005b, *ApJ*, **628**, 1070 (FKW05)
- Frazin, R. A., Vásquez, A. M., Kamalabadi, F., & Park, H. 2007, *ApJ*, **671**, L201
- Fuller, J., Gibson, S. E., de Toma, G., & Fan, Y. 2008, *ApJ*, **678**, 515
- García-Alvarez, D., et al. 2006, *ApJ*, **638**, 1028
- Golub, G. H., Heath, M., & Wahba, G. 1979, *Technometrics*, **21**, 215
- Grevesse, N., & Sauval, A. J. 1998, *Space Sci. Rev.*, **85**, 161
- Harrison, R. A., & Thompson, A. M. 1991, *Intensity Integral Inversion Techniques: a Study in Preparation for the SOHO Mission*, Technical Report RAL-91-092 (Oxfordshire: Rutherford Appleton Laboratory)
- Howard, R. A., et al. 2008, *Space Sci. Rev.*, **136**, 67
- Kashyap, V., & Drake, J. J. 1998, *ApJ*, **503**, 450
- Kiely, A., & Klimesh, M. 2003, *The ICER Progressive Wavelet Image Compressor*, IPN Progress Report 42-155 (Pasadena, CA: JPL)
- Landi, E., & Feldman, U. 2008, *ApJ*, **672**, 674
- Landi, E., & Landini, M. 1997, *A&A*, **327**, 1230
- Mariska, J. T. 1992, *The Solar Transition Region* (Cambridge: Cambridge Univ. Press)
- Pottasch, S. R. 1963, *ApJ*, **137**, 945
- Prato, M., et al. 2006, *Sol. Phys.*, **237**, 61
- Raymond, J. C., et al. 1997, *Sol. Phys.*, **175**, 645
- Schmelz, J. T., Kashyap, V. L., & Weber, M. A. 2007, *ApJ*, **660**, L157
- Schrijver, C. J., Van den Oord, G. H. J., & Mewe, R. 1994, *A&A*, **289**, L23
- Thompson, W. T. 2006, *A&A*, **449**, 791
- Vásquez, A. M., Frazin, R. A., Hayashi, K., Sokolov, I. V., Cohen, O., Manchester, W. B., & IV Kamalabadi, F. 2008, *ApJ*, **682**, 1328
- Vásquez, A. M., Frazin, R. A., & Kamalabadi, F. 2009, *Sol. Phys.*, **256**, 73
- Weber, M. A., Deluca, E. E., Golub, L., & Sette, A. L. 2004, in *Proc. IAU Symp. 223, Multi-wavelength Investigations of Solar Activity*, ed. A. V. Stepanov, E. E. Benevolenskaya, & A. G. Kosovichev (Cambridge: Cambridge Univ. Press), 321
- Young, P. R., Del Zanna, G., Landi, E., Dere, K. P., Mason, H. E., & Landini, M. 2003, *ApJS*, **144**, 135

⁸ Equation (9) of Frazin & Janzen (2002) is incorrect. The correct version is given here in Equation (E2). Since the error is a factor of $\cos \rho$ and ρ has been less than 1.6° in everything published by Frazin and colleagues so far, this error has had no practical consequences.